5. Multivalued Distributions of Hot Electrons Between Equivalent Valleys

Marion Asche

With 20 Figures

Let us consider a many-valley semiconductor (Si as a typical example) subject to an external electric field. When the intervalley transition rate increases sharply with carrier heating, transverse fluctuations of the electric field, instead of decaying spontaneously, may lead to a repopulation of the valleys, even if these are equally oriented with respect to the applied field. As a consequence, a steady state which in the absence of fluctuations is symmetric around the field direction may, owing to the fluctuations, decay into new steady states which lose this symmetry (states of broken symmetry). Under this condition, transverse to the direction of the current flow, a sample exhibits regions with different transverse fields, and in turn negative differential conductivity (NDC) may occur on account of the anisotropy in the conductivity. The position of the wall between regions with different transverse fields becomes very sensitive to external disturbances and can be switched by these influences. For the case of electrons in Si we shall show that the results obtained from different experiments and Monte Carlo calculations agree very well and fully support the evidence of this spontaneous symmetry breaking.

In Sect. 5.1 the creation of the transverse fields is analyzed for a two-valley model and the appearance of NDC is explained accordingly. Section 5.2 reports the results of an experimental proof for some predicted effects, as obtained for n-Si at low temperatures. A theoretical analysis of the conditions which allow a multivalued electron distribution (MED) to be realized is given in Sect. 5.3. Numerical results for the transverse fields and the drift velocity as functions of the heating field are presented in Sect. 5.4. In Sect. 5.5 the necessary condition for MED, that is, a sharp change of the intervalley transfer rate with carrier heating, is investigated. Section 5.6 reports further experimental investigations which were performed for other orientations of the current density different from that of Sect. 5.1. Finally, Sect. 5.7 provides a brief retrospect of the efforts made to prove the existence of MED, in view of its future possibilities.

5.1 Multivalued Electron Distribution (MED) as Spontaneous Symmetry Breaking

In systems operating under strongly nonlinear conditions, fluctuations can lead to spontaneous symmetry breaking (for a general review of this argument see [5.1]). Such a condition can be accomplished at high electric fields in the case of

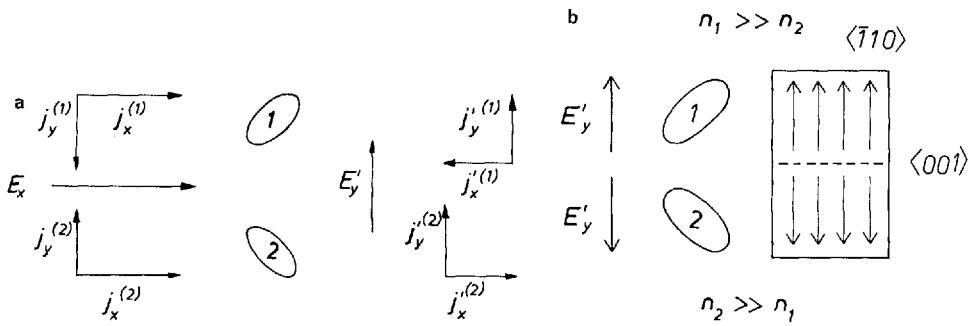

Fig. 5.1a, b. Electric fields and currents for a simple model semiconductor consisting of two equivalent valleys (**a**). Cross section in the middle of a sample with transverse fields (arrows) and carrier redistributions in the two layers (b)

many-valley semiconductors. In fact, for appropriate crystallographic orientations, the uniform distribution of a high steady-state field may become unstable when the carrier transition rate between equivalent valleys sharply increases with carrier energy, and thus with increasing field strength.

For illustrative purposes let us consider a brick-shaped sample with the two transverse dimensions much smaller than the logitudinal one, and assume a semiconductor band model consisting of two equivalent minima with ellipsoidal equienergetic surfaces (Fig. 5.1a). If we apply an electric field E_x symmetrically oriented with respect to both valleys, the components of the current density of each valley in the field direction $j_x^{(1)}$ and $j_x^{(2)}$ are equal. However, because of the anisotropic conductivity in each valley associated with the nonspherical energy surfaces, the components of the current density of each valley transverse to the field direction $j_y^{(1)}$ and $j_y^{(2)}$ are equal but oppositely oriented. The current density in each valley is therefore turned from the direction of the applied field into the direction of smaller effective mass according to $\boldsymbol{j}^{(\alpha)} = en^{(\alpha)}\boldsymbol{\mu}^{(\alpha)}\boldsymbol{E}$. Here e is the electron charge: $n^{(\alpha)}$ and $\boldsymbol{\mu}^{(\alpha)}$ denote the carrier density and mobility in valley α, respectively. The components of the mobility tensor $\boldsymbol{\mu}^{(\alpha)}$ are given by $\mu_i^{(\alpha)} = e\langle\tau_i\rangle/m_i$, with $\langle\tau_i\rangle$ the averaged ith component of the momentum relaxation time and m_i^{-1} the ith component of the inverse effective-mass tensor.

Similarly, a field fluctuation E_y' will cause parallel directed components $j_y'^{(1)}$ and $j_y'^{(2)}$ and oppositely directed components $j_x'^{(1)}$ and $j_x'^{(2)}$.

Now, to first order there are two terms which contribute to the energy fluctuation, namely, $j_y^{(\alpha)}E_y'$ and $j_y'^{(\alpha)}E_y$, originated in the fluctuating field and current, respectively. As can be easily argued from Fig. 5.1, both these contributions are negative for Valley 1 and therefore the carriers of this valley will be cooled. On the other hand, both contributions are positive for Valley 2; therefore the carriers of this valley will be heated. The resulting difference in the valley energies permits an electron redistribution between the two valleys. Consequently, when an intervalley scattering process with the assistance of a

phonon becomes possible, the hotter valley will finally be depleted. Therefore all current contributions of Valley 1 will be increased at the expense of Valley 2, and the conductivity of the two-valley semiconductor, which in the absence of fluctuations was symmetric around the field direction, will now become asymmetric.

5.1.1 States of Broken Symmetry – Layers of Transverse Fields

If $j_y^{(1)} < (j_y^{(2)} + j_y'^{(1)} + j_y'^{(2)})$, that is, the only component opposite to E_y' is smaller than the sum of the others directed parallel to E_y', the fluctuation will be damped. When, on the other hand, $j_y^{(1)} > (j_y^{(2)} + j_y'^{(1)} + j_y'^{(2)})$, the fluctuation will be enhanced and, in turn, a finite transverse field built up.

In a similar way a fluctuation of the opposite sign will cause a depletion of the population in Valley 1. In this case, a finite transverse field will be built up if the component $j_y^{(2)}$, oppositely oriented to E_y', is greater than the sum of the others directed parallel to E_y'.

Summarizing, it can be stated that if the value of the difference between the currents $j_y^{(\alpha)}$ of Valleys 1 and 2 is greater than the corresponding value of the sum of the fluctuation currents $j_y'^{(\alpha)}$, a symmetric steady state with equal electron densities of both valleys is unstable. The spontaneous symmetry breaking of the electron distribution between equivalent valleys leads to new asymmetric steady states of the semiconductor. These states are characterized by the presence of electric fields which are oppositely directed and perpendicular to the total current density j_x[1]. Since the two possible asymmetric states, respectively with higher population of Valley 1 or 2, are degenerate, the boundary conditions determine how the sample decays into regions of either of the two states. For the case reported in Fig. 5.1 theoretical considerations [5.3, 4] predict that, in absence of intervalley transfer on the surfaces with normals in y direction, the electrons populate Valley 1 on one surface and Valley 2 on the opposite one. Consequently the sample decays into layers, each with the transverse field of that sign (compare Fig. 5.1a) which belongs to the predominant population of the valley preferred by the boundary condition of the adjacent surface (Fig. 5.1b). By symmetry requirements the wall between the layers (interlayer wall) is located halfway between the surfaces if the crystal is perfectly homogeneous and the field is oriented exactly symmetrically with respect to the considered valleys.

The presence of a small additional transverse electric field[2] in the y direction will assist the development of the field fluctuation of the same sign and damp the

---

1 If the heating field is not directed along a high-symmetry axis of the crystal, the directions of the current density and field strength do not coincide, as was predicted in [5.2a] and experimentally shown for the first time in [5.2b]. In bounded samples this effect leads to transverse field components (the Sasaki field). By analogy, the appearance of transverse fields for symmetry directions was, in the beginning, called "multivalued Sasaki effect".

2 Of course, when this transverse field is higher than the fluctuation field, the latter will no longer play any role.

development of that opposite to its orientation. Therefore it will shift the interlayer wall in such a way that the layer with the field in the same direction will grow. The additional field may be caused by an inhomogeneity in the crystal, a contact, a magnetic field, a mechanical stress, etc. The shift of the interlayer wall towards one of the surfaces gives rise to a high potential difference between equivalent points 1 and 2 on the pair of opposite surfaces, as indicated in Fig. 5.2 (Sect. 5.2.1).

5.1.2 Negative Differential Conductivity (NDC) Caused by Transverse Fields

For the case of the two-valley semiconductor, the symmetry breaking may lead to a reduction of the total current density j_x along the direction of the applied field with increasing field strength. In fact, for E_y' oriented as in Fig. 5.1 with growing repopulation between the valleys, the increase of $j_x'^{(1)}$ does not compensate the change of $j_x'^{(2)}$, but both add so that the total current density j_x will be a decreasing function of field, thus leading to an N-shaped NDC region in the current-voltage characteristics.

As is well known, a state with NDC is unstable and, in this case, it will cause a domainization of the field along the x direction of the sample. For values of the applied field strength above a critical value E_{low} a static high-field domain with field strength E_{high} is built up near one of the electrodes or near an inhomogeneity and will extend through the sample with rising applied field strength E_x.

Contrary to the usual NDC, which appears in presence of a longitudinal applied field only [5.5–8], in the present case NDC is due to the presence of built-in transverse fields.

5.2 Experimental Evidence of MED

For the investigations under consideration, n-Si is chosen because it has a simple many-valley band structure and fulfills the requirements with respect to intervalley scattering processes.

The Si conduction band consists of three pairs of equivalent minima (valleys) in the $\langle 100 \rangle$ directions. Each valley is characterized by a longitudinal and transverse effective mass, $m_{\text{lo}} = 0.92\, m_0$ and $m_{\text{tr}} = 0.19\, m_0$, m_0 being the free-electron mass. If a sample is cut from a slide oriented normal to $\langle \bar{1}10 \rangle$, with j_x along the $\langle 110 \rangle$ direction the valleys in the $\langle 100 \rangle$ and those in the $\langle 010 \rangle$ directions play the roles of Valleys 1 and 2 of Fig. 5.1. At the same time, the valleys in the $\langle 001 \rangle$ direction do not interfere with the phenomena expected from the simplified model, since in the $(\bar{1}10)$ plane considered their effective masses do not depend on the field direction. As a matter of fact by increasing the energy level of the two $\langle 001 \rangle$ valleys by the application of an uniaxial pressure it can be proven that their influence is not essential indeed [5.9].

Now a strong nonlinearity of the system, which is the necessary condition for symmetry breaking [5.1], can be realized by phonon-assisted intervalley

scattering of hot electrons, since the scattering rate increases exponentially with carrier energy at low temperatures. This condition, because of a lower intervalley scattering rate at ionized impurities, is more favorably met in n-Si than in n-Ge.

5.2.1 Evidence for Layered Structures

An experimental proof of the stratification of the transverse fields due to MED for a field applied along a ⟨110⟩ direction can be obtained by measuring the potential differences between adjacent Probes 1–3–2 or 1–4–2, respectively (Fig. 5.2, insert). These measurements exhibit a high positive value of the voltage between Probes 1 and 3 and a high negative value between Probes 3 and 2. Accordingly, between Probes 1 and 2 a small value remains only, which agrees with the partial compensation of the opposite fields (compare Fig. 5.1b). As an example, for one sample at $E_x = 105$ V/cm, with U_{ij} denoting the potential difference between Probes i and j, and d_{ij} their distance, the values are $\Delta U_{13}/d_{13} = 47.6$ V/cm, $\Delta U_{32}/d_{32} = -44.6$ V/cm, and $\Delta U_{12}/d_{12} = 3$ V/cm. Quantitatively, the same picture is obtained with Probe 4 replacing Probe 3. In this way it can be shown that, above a critical value of the applied field strength, the small voltage which appears between Probes 1 and 2 on the $(\bar{1}10)$ surfaces (× × × in Fig. 5.2) can be ascribed to the difference of the two opposite transverse fields.

A magnetic field $\boldsymbol{B}$ in the ⟨001⟩ direction creates a Hall field parallel to the $\langle\bar{1}10\rangle$ direction and, as mentioned in Sect. 5.1.1, this field shifts the interlayer wall in such a way that the layer with the transverse field in the direction of the Hall field will grow [5.3,4,10,11]. Figure 5.2 shows the transverse voltage difference between Probes 1 and 2 normalized to the width of the sample as a function of the heating field applied in the absence of $\boldsymbol{B}$ and for $B = \mp 0.066$ T. For values of E_x

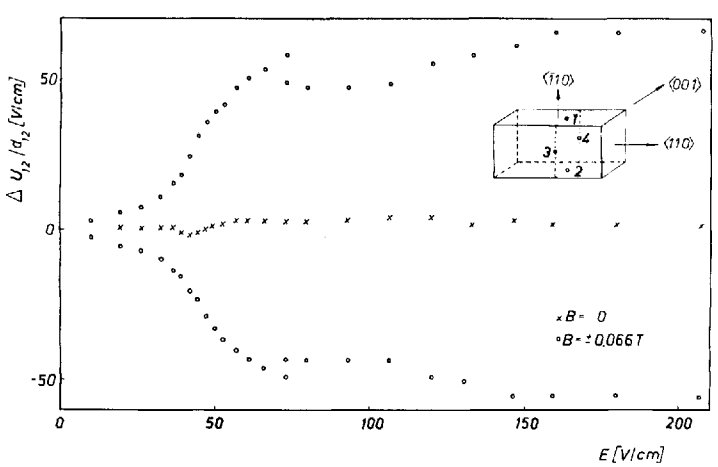

Fig. 5.2. Transverse fields versus applied fields with and without magnetic field for n-Si at 27 K. *Insert*: crystallographic orientation of the sample and position of the probes

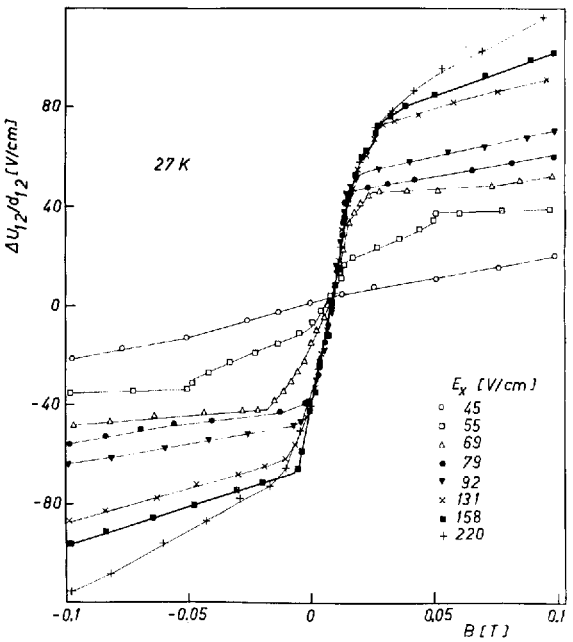

Fig. 5.3. Transverse fields versus magnetic field for n-Si at 27 K. Values of the applied field are indicated in the figure

lower than 40 V/cm a usual Hall field is observed. Above 40 V/cm [3], the value of the transverse field exhibits an anomalous steep increase while the longitudinal static high-field domain (Sect. 5.2.2) is found to extend further into the sample, with a value which remains nearly constant for an applied electric field above E_{high}. The behavior is almost symmetric with respect to a change in the polarity of the magnetic field. If in the absence of the magnetic field the interlayer wall is not located in the middle of the sample, but a significant potential difference between the probes on the pair of $(\bar{1}10)$ surfaces is already present, then only one type of the magnetic field polarity switches the wall remarkably, i.e., the polarity for which the wall is shifted to the opposite surface. In this case, too, the transverse potential difference remains equal, but opposite in sign according to the polarity of $\boldsymbol{B}$ [Ref. 5.11, Fig. 1].

A detailed analysis of $\Delta U_{12}/d_{12}$ as a function of $\boldsymbol{B}$ is shown in Fig. 5.3. Here for fields applied below 40 V/cm the common Hall effect is observed. Above a critical value of the applied field E_x, 45 V/cm in the figure at weak B $\Delta U_{12}/d_{12}$ exhibits a steep rise. At applied field values above E_{high} (about 79 V/cm for this sample) and in the same region of weak B, the slope of all curves remains almost constant with increasing applied field, that is, as long as MED is realized (thick line in Fig. 5.3). Always for fields above E_{high}, by increasing the magnetic field an

3 In presence of longitudinal domains of high- and low-field strength, E_x corresponds to the applied potential divided by the length of the sample.

abrupt transition towards a weaker dependence of the transverse field is observed; this corresponds to the fact that the interlayer wall has already been shifted to one of the surfaces. For $E_x \gtrsim 200$ V/cm this abrupt transition is smoothed out, indicating that there is no spontaneous symmetry breaking of the equivalent valleys left, but only an anomalously high carrier redistribution between them. This means that the Hall field is strongly enhanced by the intervalley redistribution of the electrons, which in turn is due to the different influence the Hall field has on carrier heating in both valleys [5.12]. While the increase at weak magnetic fields is jumplike due to the layered structure, the increase with $\boldsymbol{B}$ becomes smoother for the homogeneous case in the absence of MED. Of course, for high $\boldsymbol{B}$, when in the case of MED the interlayer wall has already been shifted to the surface, the redistribution is similar for both cases.

5.2.2 Current Saturation and Longitudinal Domains

Another consequence of MED is the reduction of the current density along the applied field, mentioned in Sect. 5.1.2, which can lead to an NDC region and in turn to a domainization of the sample. This phenomenon was observed in [5.11, 13] as a saturation of the current density, which occurs in a certain region of values of the field strengths applied along a ⟨110⟩ direction as shown in Fig. 5.4 (Curve *a*). The critical field strength E_{low}, for which a high-field domain appears at one contact, is clearly exhibited.

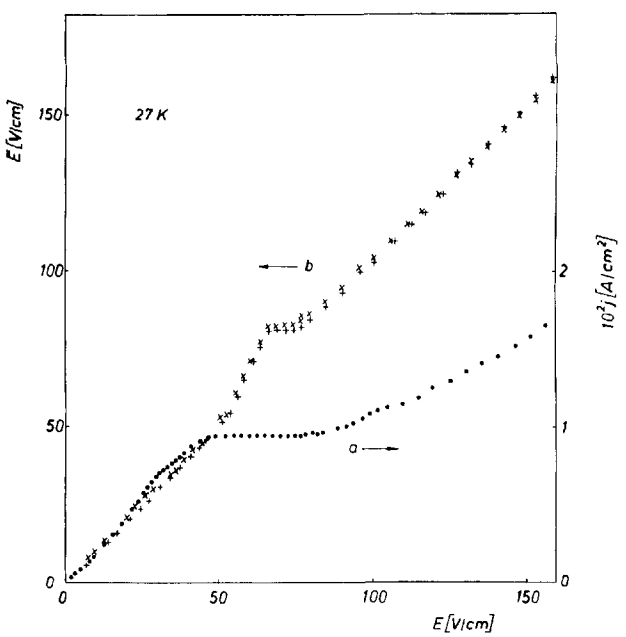

Fig. 5.4. Current density (*a*) and longitudinal fields (*b*) at the Probes 3 (×) and 4 (+) (*insert* of Fig. 5.2) versus applied field

The domainization of the longitudinal field is to be seen by the behavior of the averaged field strength $\bar{E}$ between the current contact at low potential and probes at the (001) surfaces (Curves *b* in Fig. 5.4). It should be noted that the probes are approximately situated halfway between the $(\bar{1}10)$ surfaces to minimize the influences from the transverse fields [5.11]. When the current begins to saturate, the two curves (*b*) show a superlinear rise of the field strength at these probes. This corresponds to the buildup of a static high-field domain at the current contact [5.14]. Then the two curves (*b*) exhibit a plateau. This means that the high-field domain has already reached the position of the probes and extends further into the direction of the other current contact. When the high-field domain reaches this contact, the field strength in the whole sample rises by further increasing the applied field. Also the inverse effect, which corresponds to a domain nucleated near the current contact at the higher potential, is often observed.

5.3 Theoretical Analysis of MED (Homogeneous Case)

Following [5.3, 15] an analytical theory can be developed by introducing the following simplifying assumptions:

(1) In each valley α ($\alpha = 1, 2, 3$) the carrier distribution function $f^{(\alpha)}(\boldsymbol{k})$ only weakly deviates from the isotropic part $f_0^{(\alpha)}$ ($\mathscr{E}$).

(2) Transitions between perpendicular valleys (f-type scattering), characterized by an out scattering time $\tau^{(\alpha)}$, have negligible effects for the energy and momentum balance and only determine the valley population, thus leading to an electron density in the valley given by

$$n^{(\alpha)} = n\tau^{(\alpha)} \Big/ \sum_{\beta=1}^{3} \tau^{(\beta)}. \tag{5.1}$$

(3) A momentum relaxation time can be introduced, the anisotropy of which is independent of carrier energy $\mathscr{E}$, thus allowing the mobility of the valley α to be written as

$$\begin{aligned} \boldsymbol{\mu}^{(\alpha)} &= \boldsymbol{a}^{(\alpha)} \mu(E^{(\alpha)}) \\ a_{ij}^{(\alpha)} &= g_{ik}^{(\alpha)} g_{jk}^{(\alpha)} M_{kk}, \end{aligned} \tag{5.2}$$

where sum over repeated indices is implied. Here $[g^{(\alpha)}]$ is the matrix transforming[4] the principal axes of each valley to the reference frame of the sample; $\boldsymbol{M} = 3\boldsymbol{\mu}/(2\mu_{\mathrm{tr}} + \mu_{\mathrm{lo}})$ is a dimensionless diagonal tensor with $\mu_{11} = \mu_{\mathrm{lo}}$ and $\mu_{22} = \mu_{33} = \mu_{\mathrm{tr}}$.

4 It consists of the transformation $[B^{(\alpha)}]$ from the axes of the valley to the main crystallographic axes and $[A]$ from them to the reference frame of the sample.

Now $\mu(E^{(\alpha)})$ and $\tau^{(\alpha)}=\tau(E^{(\alpha)})$ depend only on the effective field strength $\boldsymbol{E}^{(\alpha)}$ given by $E^{(\alpha)2}=\boldsymbol{E}\boldsymbol{a}^{(\alpha)}\boldsymbol{E}$; the latter ones are reduced to the usual expressions in the case of an isotropic momentum relaxation time [5.16].

For a homogeneous brick-shaped sample with the two transverse dimensions d_y and d_z smaller than the longitudinal one, the definition of the current density

$$\boldsymbol{j}=en\sum_{\alpha}\tau(E^{(\alpha)})\mu(E^{(\alpha)})\boldsymbol{a}^{(\alpha)}\boldsymbol{E}\Big/\sum_{\beta}\tau(E^{(\beta)}) \tag{5.3a}$$

and the conditions $j_y=j_z=0$ yield

$$j_x=en\sum_{\alpha}\phi^{(\alpha)}a_{xi}^{(\alpha)}E_i\Big/\sum_{\beta}\tau(E^{(\beta)}). \tag{5.3b}$$

With $\phi^{(\alpha)}$ abbreviating $\mu(E^{(\alpha)})\tau(E^{(\alpha)})$, for $\vartheta_y=E_y/E_x$ and $\vartheta_z=E_z/E_x$ the following expressions are obtained:

$$\vartheta_y=-\frac{\sum_{\alpha}\phi^{(\alpha)}a_{yx}^{(\alpha)}\sum_{\beta}\phi^{(\beta)}a_{zz}^{(\beta)}-\sum_{\alpha}\phi^{(\alpha)}a_{zx}^{(\alpha)}\sum_{\beta}\phi^{(\beta)}a_{yz}^{(\beta)}}{\sum_{\alpha}\phi^{(\alpha)}a_{yy}^{(\alpha)}\sum_{\beta}\phi^{(\beta)}a_{zz}^{(\beta)}-\sum_{\alpha}\phi^{(\alpha)}a_{zy}^{(\alpha)}\sum_{\beta}\phi^{(\beta)}a_{yz}^{(\beta)}}$$

$$\vartheta_z=\frac{\sum_{\alpha}\phi^{(\alpha)}a_{yx}^{(\alpha)}\sum_{\beta}\phi^{(\beta)}a_{zy}^{(\beta)}-\sum_{\alpha}\phi^{(\alpha)}a_{zx}^{(\alpha)}\sum_{\beta}\phi^{(\beta)}a_{yy}^{(\beta)}}{\sum_{\alpha}\phi^{(\alpha)}a_{yy}^{(\alpha)}\sum_{\beta}\phi^{(\beta)}a_{zz}^{(\beta)}-\sum_{\alpha}\phi^{(\alpha)}a_{zy}^{(\alpha)}\sum_{\beta}\phi^{(\beta)}a_{yz}^{(\beta)}}. \tag{5.4}$$

5.3.1 General Discussion: The Case of Si with Current Density in a $(\bar{1}10)$ Plane

Since the analytical expressions for a general orientation become too complicated to allow clear insight into the expected effects and because available experimental data for Si refer to the case of a current density in a $(\bar{1}10)$ plane, the following analysis will be limited to this case.

By indicating with ψ the angle between the $\langle 110\rangle$ direction and the current density vector (Fig. 5.5), for the nonvanishing terms of (5.2) one obtains

$$a_{xx}^{(1)}=a_{xx}^{(2)}=1+a_1(1-3\cos 2\psi)/4,$$

$$a_{xx}^{(3)}=1-a_1(1-3\cos 2\psi)/2,$$

$$a_{xy}^{(1)}=-a_{xy}^{(2)}=3a_1(\cos\psi)/2,\quad a_{xz}^{(1)}=a_{xz}^{(2)}=3a_1(\sin 2\psi)/4,$$

$$a_{xz}^{(3)}=-3a_1(\sin 2\psi)/2,\quad a_{yy}^{(1)}=a_{yy}^{(2)}=1-a_1/2,$$

$$a_{yy}^{(3)}=1+a_1,\quad a_{yz}^{(1)}=-a_{yz}^{(2)}=-3a_1(\sin\psi)/2,$$

$$a_{zz}^{(1)}=a_{zz}^{(2)}=1+a_1(1+3\cos 2\psi)/4,$$

$$a_{zz}^{(3)}=1-a_1(1+3\cos 2\psi)/2$$

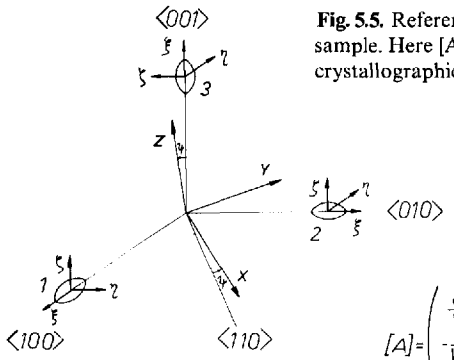

Fig. 5.5. Reference axes in the valleys and reference frame of the sample. Here [A] represents the matrix for the transition between crystallographic axes and sample reference frame

$$[A]=\begin{pmatrix} \frac{\cos\Psi}{\sqrt{2}} & \frac{\cos\Psi}{\sqrt{2}} & \sin\Psi \\ -\frac{1}{\sqrt{2}} & \frac{1}{\sqrt{2}} & 0 \\ -\frac{\sin\Psi}{\sqrt{2}} & -\frac{\sin\Psi}{\sqrt{2}} & \cos\Psi \end{pmatrix}$$

with $a_1=(\mu_{tr}-\mu_{lo})/(2\,\mu_{tr}+\mu_{lo})$. Introducing

$$\begin{aligned} \Phi_0&=(\phi^{(1)}-\phi^{(2)})/\sum_\alpha \phi^{(\alpha)} \\ \Phi\ &=(\phi^{(1)}+\phi^{(2)}-2\,\phi^{(3)})/\sum_\alpha \phi^{(\alpha)} \end{aligned} \tag{5.5}$$

the total current density is

$$\begin{aligned} j_x=en\sum_\alpha \phi^{(\alpha)}&[1+\Phi a_1(1-3\cos 2\psi)/4+\vartheta_y\Phi_0 3a_1(\cos\psi)/2 \\ &+\vartheta_z\Phi 3a_1(\sin 2\psi)/4]\,E_x/\sum_\alpha \tau^{(\alpha)}. \end{aligned} \tag{5.6}$$

The ratios of the transverse fields to the applied field are

$$\begin{aligned} \vartheta_y&=-\frac{\Phi_0 3a_1\{\cos\psi[4+\Phi a_1(1+3\cos 2\psi)]+\Phi 3a_1\sin 2\psi\sin\psi\}}{2\{(1-\Phi a_1/2)\,[4+\Phi a_1(1+3\cos 2\psi)]-(\Phi_0 3a_1\sin\psi)^2\}}, \\ \vartheta_z&=-\frac{(\Phi_0 3a_1)^2\cos\psi\sin\psi+\Phi 3a_1(1-\Phi a_1/2)\sin 2\psi}{(1-\Phi a_1/2)\,[4+\Phi a_1(1+3\cos 2\psi)]-(\Phi_0 3a_1\sin\psi)^2}, \end{aligned} \tag{5.7}$$

and the arguments $E^{(\alpha)}$ of the $\phi^{(\alpha)}$ are given by

$$\begin{aligned} \boldsymbol{E}\boldsymbol{a}^{(1)}\boldsymbol{E}&=\{1+a_1(1-3\cos 2\psi)/4+\vartheta_y 3a_1\cos\psi+\vartheta_z 3a_1(\sin 2\psi)/2 \\ &\quad+\vartheta_y^2(2-a_1)/2-\vartheta_y\vartheta_z 3a_1\sin\psi+\vartheta_z^2[1+a_1(1+3(\cos 2\psi))/4]\}E_x^2, \\ \boldsymbol{E}\boldsymbol{a}^{(3)}\boldsymbol{E}&=\{1-a_1(1-3\cos 2\psi)/2-\vartheta_z 3a_1\sin 2\psi+\vartheta_y^2(1+a_1) \\ &\quad+\vartheta_z^2[1-a_1(1+3\cos 2\psi)/2]\}E_x^2, \end{aligned} \tag{5.8}$$

where for $\boldsymbol{E}\boldsymbol{a}^{(2)}\boldsymbol{E}$ only terms proportional to ϑ_y change their signs in comparison to $\boldsymbol{E}\boldsymbol{a}^{(1)}\boldsymbol{E}$.

Inserting (5.8) into (5.7) these equations may be written in the form

$$\vartheta_y = R(\vartheta_y, \vartheta_z),$$
$$\vartheta_z = Q(\vartheta_y, \vartheta_z). \tag{5.9}$$

Eq. (5.9) have to be discussed with respect to the possibility of MED. They are strongly nonlinear, of transcendent type, and their right-hand sides are limited; furthermore, they always have the common solutions corresponding to the Sasaki effect [5.2].

From (5.7) it is to be seen that for $\psi = \pi/2$ (the $\langle 001 \rangle$ direction) only the solution $\vartheta_y = \vartheta_z = 0$ exists; thus no MED can appear with a field applied along this direction.

For $\psi = 0$ (the $\langle 110 \rangle$ direction) the z component again only has the solution $\vartheta_z = 0$, but ϑ_y reads

$$\vartheta_y = -\frac{3a_1(\phi^{(1)} - \phi^{(2)})}{(2-a_1)(\phi^{(1)} + \phi^{(2)}) + 2(1+a_1)\phi^{(3)}}. \tag{5.10}$$

Besides the trivial solution $\vartheta_y = 0$, which corresponds to $\phi^{(1)} = \phi^{(2)}$ – that is, equal population of Valleys 1 and 2 – there may be nontrivial solutions with nonsymmetric population of the Valleys 1 and 2, this because for $\vartheta_y \neq 0$ the effective fields differ for both valleys, as can be seen from (5.8).

For $\tan \psi = 1/\sqrt{2}$ (the $\langle 111 \rangle$ direction) the trivial solutions of (4.7) $\vartheta_y = \vartheta_z = 0$ mean equal population of all valleys, see (5.5). Further on, nontrivial solutions with nonsymmetric population of the valleys may exist.

For other orientations besides the common nonvanishing solutions, nontrivial ones can exist, too.

The nontrivial solutions for ϑ_y or ϑ_z lead to a conductivity which decreases with increasing applied field. Furthermore for ϑ_y and ϑ_z increasing strongly with E_x, even NDC can be obtained (detailed conditions were reported in [5.15]).

To carry out the analysis of the nontrivial solutions for each E_x the left- and right-hand sides of (5.9) can be drawn as functions of ϑ_y and ϑ_z, and their intersections determined.

5.3.2 Current Density Along a $\langle 110 \rangle$ Direction

An example of the above-mentioned procedures is illustrated in Fig. 5.6 for the case of a current density along a $\langle 110 \rangle$ direction. Under this configuration only one of the transverse field components in (5.9) does not vanish. The critical-field strengths for a nontrivial solution are given when the curves, according to the left- and right-hand sides of (5.10), are touching; this means that their slopes

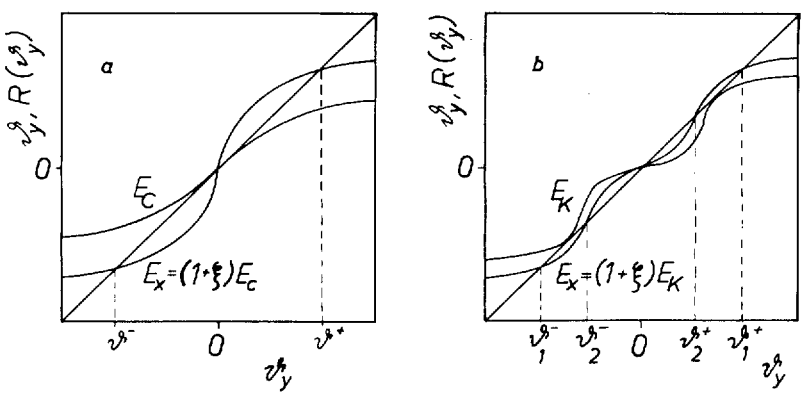

Fig. 5.6a, b. Both sides of (5.10) as functions of ϑ_y near the critical electric fields of E_C type (**a**), and of E_K type (**b**)

have to be equal:

$$1=\frac{dR(\vartheta_y)}{d\vartheta_y}. \tag{5.11}$$

If this occurs in the vicinity of $\vartheta_y=0$ (Fig. 5.6a), one obtains

$$\phi^{(1)}=\phi^{(2)} \quad \text{and} \quad \frac{d\phi^{(1)}}{d\vartheta_y}=-\frac{d\phi^{(2)}}{d\vartheta_y}=\frac{3a_1E_x}{\sqrt{2(2-a_1)}}\frac{d\phi(E^{(1)})}{dE^{(1)}}, \tag{5.12}$$

and the use of (5.11) with $E^{(1)}=\sqrt{2(2-a_1)}\,E_x/2=E_C$ leads to

$$-\frac{9a_1^2}{(2-a_1)^2}\frac{E_C}{\phi(E_C)}\frac{d\phi(E_C)}{dE_C}=1+\frac{(1+a_1)}{(2-a_1)}\frac{\phi(\sqrt{2(1+a_1)/(2-a_1)}\,E_C)}{\phi(E_C)}$$

or

$$-\left(\frac{\mu_{tr}-\mu_{lo}}{\mu_{tr}+\mu_{lo}}\right)^2\frac{d\ln\phi(E_C)}{d\ln E_C}=1+\frac{\mu_{tr}\phi(\sqrt{2\mu_{tr}/(\mu_{tr}+\mu_{lo})}\,E_C)}{(\mu_{tr}+\mu_{lo})\phi(E_C)}. \tag{5.13}$$

The condition for the existence of a pair of nontrivial solutions $\vartheta^{\pm}$ can be fulfilled if $\phi^{(\alpha)}=\mu(E^{(\alpha)})\tau(E^{(\alpha)})$ exhibits a pronounced decrease with increasing fields. Since $\mu(E^{(\alpha)})$ is a slowly varying function, the required steep change of $\phi^{(\alpha)}$ with E_x depends critically on the intervalley scattering time $\tau(E^{(\alpha)})$.

When more solutions exist we have to decide whether they are stable or unstable. These investigations were performed in [5.15], and here only the results are used.

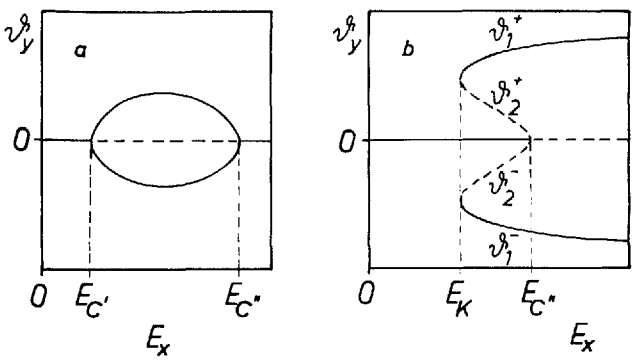

Fig. 5.7a, b. Possible values of the ratio of transverse to applied electric fields versus fields applied along a ⟨110⟩ direction

To discuss the behavior of ϑ_y in the neighborhood of the critical point ($\vartheta_y = 0$, $E_x = E_C$) we insert $E_x = E_C(1+\xi)$ into (5.8) and develop in a power series $\phi^{(\alpha)}$ with respect to ϑ_y and ξ. To the first nonvanishing order in ϑ_y and ξ, this leads to a relation of the type [5.15, 17]

$$\vartheta_y[B(E_C)\xi + \vartheta_y^2 A(E_C)] = 0. \tag{5.14}$$

When $A(E_C)$ and $B(E_C)$ have different signs, a pair of nontrivial solutions $\vartheta^{\pm} = \pm\sqrt{B(E_C)\xi/A(E_C)}$ is obtained for positive ξ, and the critical-field strength is termed $E_{C'}$. When they have the same sign, $\vartheta^{\pm}$ is obtained for negative ξ, and the critical-field strength is designated as $E_{C''}$. Figure 5.7a illustrates the dependence of $\vartheta^{\pm}$ on E_x, if $E_{C'}$ and $E_{C''}$ are the minimum and maximum field strength for MED, respectively. The broken lines indicate the nonstable solutions and the solid lines the stable ones, respectively [5.15].

If, however, $E_{C''}$ (i.e., $\xi < 0$) is realized for the lower limit of the field region with MED, in the vicinity of $\vartheta_y = 0$ the function $R(\vartheta_y)$ becomes more complicated. Then a critical-field strength E_K (Fig. 5.6b) exists for which at once two pairs of additional solutions, besides the trivial one, appear at $\vartheta_y \neq 0$ (in contrast with a critical field of E_C type, with one pair of nontrivial solutions in the vicinity of $\vartheta_y = 0$). This case is shown in Fig. 5.7b, the higher pair of values for the intersection of ϑ_y and $R(\vartheta_y)$ corresponds to stable solutions $\vartheta_1^{\pm}$, while the lower pair $\vartheta_2^{\pm}$ corresponds to unstable solutions. If we obtain two pairs of solutions for $E_x > E_K$, then, by further increasing the heating field, $\vartheta_2^{\pm}$ shifts towards $\vartheta_y = 0$ (as may be seen from Fig. 5.6b) and only one pair of nontrivial solutions will remain for fields above $E_{C''}$. A similar situation can appear for the high-field limit of the region with nontrivial solutions ϑ_y, but mixed types of Fig. 5.7a and b, may be found for the upper and lower limit of the critical-field region.

The situation above described remains valid for values of ψ which correspond to directions close to ⟨110⟩, since the electron density in the group of

Valleys 1 and 2 essentially does not change when compared to that of the Valleys 3[5]. At increasing values of ψ, the influence of Valleys 3 on MED increases (remember $\phi^{(1)}=\phi^{(2)}=\phi^{(3)}$ for $\tan\psi=1/\sqrt{2}$ in the absence of MED) and instead of the MED between Valleys 1 and 2, now a redistribution of the carriers among all three pairs of valleys has to be considered. For this case to occur, the limiting value of ψ depends on the values of the microscopic parameters used, and it can be determined by a quantitative theory only.

5.3.3 Current Density Along a ⟨111⟩ Direction

When the current density is along or close to a ⟨111⟩ direction, a simple analytical theory is not available for the general case. However, it is possible to treat the problem when either $\vartheta_y=0$ or $\vartheta_z=0$, that is, by shunting one of the transverse field components. The condition $\vartheta_z=0$ leads to solutions for ϑ_y which, when compared with the case of the ⟨110⟩ direction, differ only quantitatively. On the other hand, the condition $\vartheta_y=0$ offers the possibility of investigating the conditions of MED on account of ϑ_z, that is, when a redistribution of carriers between the Valleys 3 and the group of Valleys 1 and 2 takes place. This case leads to new types of solutions. In particular, for the total current density along the ⟨111⟩ direction (5.7) yields

$$\vartheta_z=-\frac{\sqrt{2}\,a_1(\phi^{(1)}-\phi^{(3)})}{(2+a_1)\phi^{(1)}+(1-a_1)\phi^{(3)}}, \tag{5.15}$$

with the arguments of $\phi^{(\alpha)}$ equal to

$$\begin{aligned} E^{(1,2)}&=\sqrt{1+2^{1/2}a_1\vartheta_z+(1+a_1/2)\vartheta_z^2}\,E_x,\\ E^{(3)}\ &=\sqrt{1-2^{3/2}a_1\vartheta_z+(1-a_1)\vartheta_z^2}\,E_x. \end{aligned} \tag{5.16}$$

In complete analogy to the discussion for the case of the ⟨110⟩ direction, as a criterion for the appearance of MED in the vicinity of $\vartheta_z=0$, one obtains

$$1=-a_1^2\frac{d\phi^{(\alpha)}}{dE_S}\frac{E_S}{\phi^{(\alpha)}}=-a_1^2\frac{d\ln\phi^{(\alpha)}}{d\ln E_S}, \tag{5.17}$$

with $E_S=E^{(1,2)}=E^{(3)}$. Very close to the point ($\vartheta_z=0$, $E_x=E_S$), the solution of (5.15) has the form [5.15]

$$\vartheta_z[\vartheta_z-C(E_S)\xi]=0, \tag{5.18}$$

---

5 For the same reason we do not expect MED near a ⟨001⟩ direction, although from (5.4) MED could be possible.

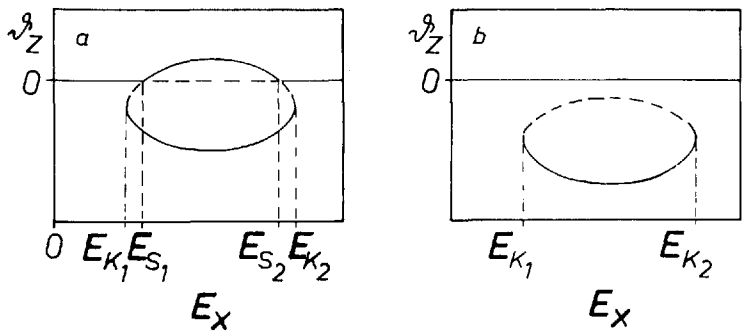

Fig. 5.8a, b. Possible values of the ratio of the transverse electric field component E_z to the applied field E_x versus fields applied along a ⟨111⟩ direction

which, in contrast with (5.14), exhibits the same number of solutions for both sides of $E_S(\xi \gtrless 0)$, as shown in Fig. 5.8a. The critical-field strengths E_K for the lower and upper limits of the region with MED are again given by the intersection of the left- and right-hand side of (5.15) for $\vartheta_z = 0$. While the upper branch, limited between E_{S_1} and E_{S_2}, represents the stable solution related to a predominant population of the group of the Valleys 1 and 2, the lower branch, limited between E_{K_1} and E_{K_2}, exhibits the stable solution $\vartheta_z < 0$, which is related to a predominant population of the Valleys 3.

Instead of the situation shown in Fig. 5.8a, an isolated closed loop $\vartheta_z(E_x)$ can be obtained (Fig. 5.8b). This means that owing to a predominant population of the Valley 3, a stable as well as an unstable nontrivial solution will appear[6], while the trivial solution remains stable for all fields. Depending on the parameters involved, type *a* or *b* of Fig. 5.8 will be realized.

Since the peculiarities corresponding to the nontrivial solutions for ϑ_y or ϑ_z show up in the current-voltage behavior, one can even obtain isolated loops theoretically for $j_x(E_x)$.

5.4 Quantitative Calculations for the Case of Si

While by analytical calculations general conclusions may be drawn for high-symmetry directions only, numerical calculations will not suffer this restriction. Thus, in the following, some numerical calculations obtained for the case of Si will be briefly reviewed.

6 When one does not choose the special brick-shaped sample geometry with $\vartheta_y = 0$, the Valleys 3 are not distinguished from the others and the problem has a threefold symmetry; in this case, any one of the valleys can become predominantly populated.

5.4.1 Monte Carlo Calculations of Intervalley Scattering Time and Effective Mobility

To evaluate $\vartheta(E_x)$ and $j_x(E_x)$ we must first calculate $\mu(E^{(\alpha)})$ and $\tau(E^{(\alpha)})$. This can be performed by the Monte Carlo method and the results obtained in this way can be used for all orientations if the effective-field method is applied[7].

Intravalley as well as intervalley scattering mechanisms have been taken into account. For intravalley scattering, the long-wavelength acoustic phonons and ionized impurities have been considered and found to be of great importance. For intervalley scattering, we recall that there are processes between the pair of valleys on the same axis (g type) and between valleys on perpendicular axes (f type). The calculations [5.15, 17–19] were performed using the values from [5.20] as reported in Table 5.1. However, to simplify calculations for f processes the interactions with the LA and TO phonons were combined (by choosing values of the phonon energy and coupling constant representative for them both). Furthermore, the interactions with the TA phonon, which owing to its low energy can play a significant role at low temperatures even if its deformation potential constant is weak, was accounted for by a variable coupling strength given by $\eta \times 0.15 \times 10^8$ eV/cm with η as an adjustable parameter. In addition, intervalley scattering at ionized impurities is included by an energy-independent relaxation time τ_0 (intervalley impurity scattering time).

Table 5.1. Parameters of intervalley phonons in Si [5.20]

Type	Branch	$\hbar\omega_j$[meV]	T_j[K]	D_{jk}[10^8 eV/cm]
g	LO ($\Delta_{2'}$)	62	720	7.5
f	TO (S_1)	59	684	2
f	LA (S_1)	47	545	4.3
f	TA (S_4)	18	210	0.15
g	TA (Δ_5)	12	140	0.65

Figure 5.9 shows the scattering rate τ^{-1} for the f-intervalley phonons as a function of the effective field at 27 K. As expected, the scattering at TA phonons predominates in the region of low fields, while processes from LA and TO phonons become prevailing in the high-field region. The influence of g-type processes on the f-intervalley electron transfer is shown in the insert for the case of coupling between electrons and g-TA phonons (again, the continous and dashed lines refer to TA and LA plus TO phonons, respectively).

7 The method of the effective fields, however, requires us to substitute the anisotropic scattering probabilities with some effective probabilities, which only depend on the angle between the initial and final momenta of the carrier. This approximation is usually found to be satisfactory.

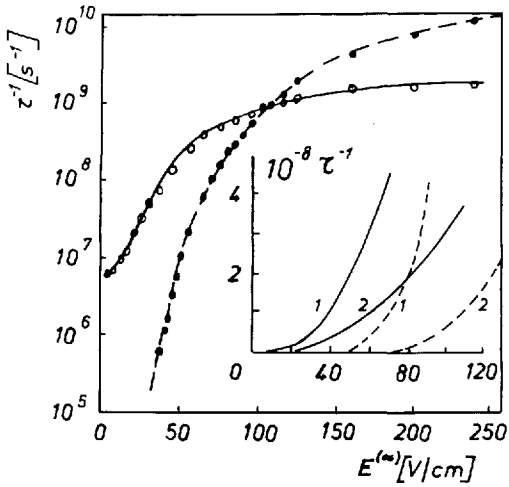

Fig. 5.9. Reciprocal scattering time of f-type intervalley processes versus effective field for TA phonons (○○○) and LA plus TO phonons (●●●) *Insert:* influence of g scattering with TA phonons on τ^{-1}: (*1*) $D_{TA}^{(g)} = 6.5 \times 10^7$ eV/cm; (*2*) $D_{TA}^{(g)} = 1.3 \times 10^8$ eV/cm

As a check of the model used, we have found that the mobility obtained from the results of Monte Carlo calculations [5.15, 17, 18] agrees with the experimental values extrapolated from time-of-flight measurements (Chap. 3).

5.4.2 Numerical Results for the Transverse Fields

With the results of Sect. 5.4.1 we are now in the position to calculate $\vartheta_y(E_x)$ and $v_x(E_x)$ [5.15, 17–19]. The results for the ⟨110⟩ case are presented in Figs. 5.10a, and b for different values of η and τ_0^{-1}. When the results are compared with the experimental data of Figs. 5.2, 4, we conclude that small values of η have to be chosen depending on the value of the additional intervalley impurity scattering. This is because experimental results do not exhibit a pronounced "camel back" behavior for ϑ_y, and only a single region, with a current density which decreases at increasing E_x, is observed. An analysis of the effect which ionized impurities produce on the intervalley scattering shows that ionized impurities determine the lower limit of E_x for MED and their effect has to be included in order to achieve agreement with experimental data. For instance, the choice of values $\eta \simeq 0.1$ and $\tau_0^{-1} \simeq 10^7\ s^{-1}$ allows us to describe the observed effects satisfactorily. The values so obtained for $D_{TA}^{(f)}$ and τ_0^{-1} are reasonable with respect to the known properties of n-Si.

The numerical results for $\vartheta_z(E_x)$, for the case when the current density is in a direction very close to the ⟨111⟩ direction, are reported in Fig. 5.11 for different values of $\delta\psi$, where $\psi = \psi_0 + \delta\psi$ with $\tan\psi_0 = 1/\sqrt{2}$. The calculations have been performed with $\eta = 0.1$ and $\tau_0^{-1} = 2 \times 10^6\ s^{-1}$. The curve in the lower part of the figure refers to the nontrivial solution for $\delta\psi = 0$ (i.e., for the ⟨111⟩ direction), and is a closed loop in accordance with Fig. 5.8b. For values of $\delta\psi$ which correspond to angular deviations less than 1° in both directions (Curves 2 and 3

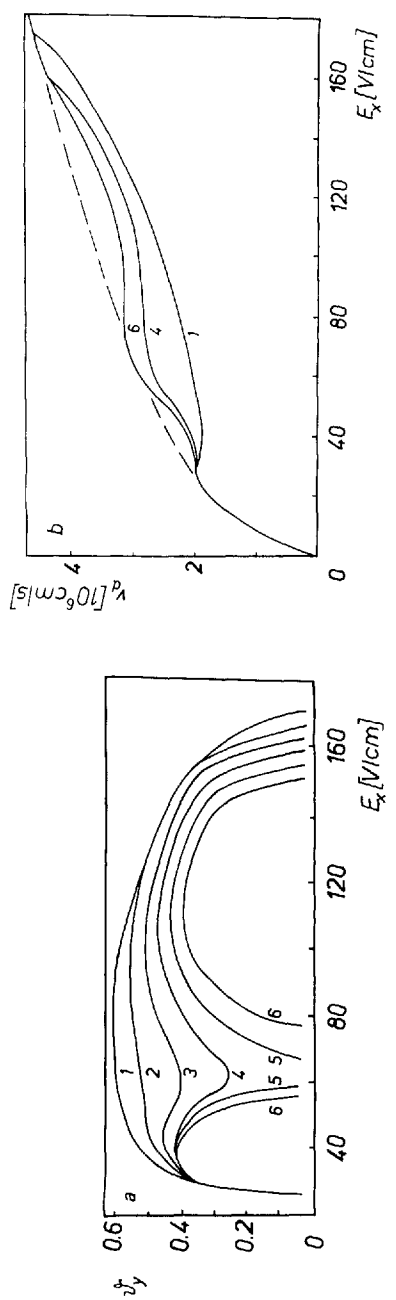

Fig. 5.10a, b. Calculated values of $\vartheta_y = E_y/E_x$ (**a**) and drift velocity (**b**) versus E_x applied along the $\langle 110 \rangle$ direction. *Upper figure* refers to $\tau_0^{-1} = \infty$ and $\eta = 0.1$ (*1*), 0.2 (*2*), 0.3 (*3*), 0.6 (*4*), 0.8 (*5*), 1.0 (*6*). *Lower figure* refers to $\eta = 0.1$ and $\tau_0^{-1} = 5 \times 10^5$ (*1*), 2×10^6 (*2*), 8×10^6 (*3*), 3.2×10^7 (*4*)

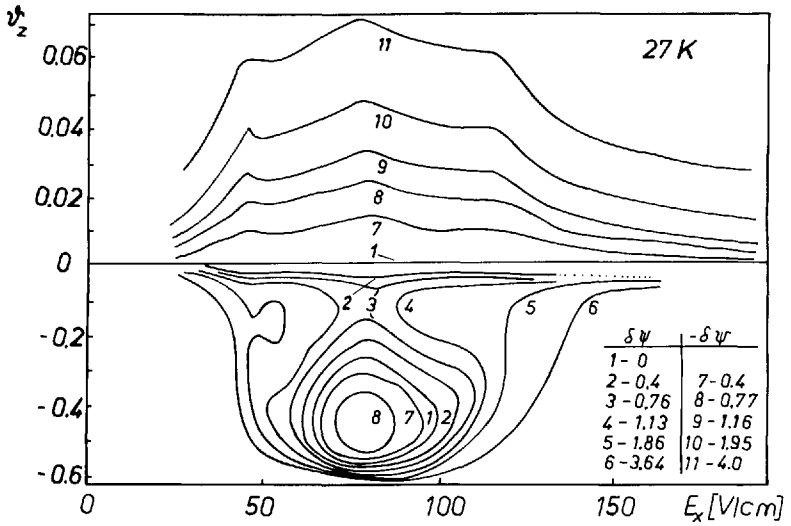

Fig. 5.11. Calculated values of $\vartheta_z = E_z/E_x$ versus E_x applied near the $\langle 111 \rangle$ direction for $\psi = \psi_0 + \delta\psi$ with $\psi_0 = 35.25°$

for ψ departing from ψ_0 towards the $\langle 001 \rangle$ direction and Curves 7 and 8 for ψ departing from ψ_0 towards the $\langle 110 \rangle$ direction) closed loops are still found, but, in addition solutions with opposite signs become available (as reported in the upper part of Fig. 5.11). These additional solutions are due to the usual Sasaki effect according to the carrier redistribution into the Valleys 3 or into the group of Valleys 1 and 2, respectively. For deviations greater than 1°, closed loops disappear for $\delta\psi < 0$, i.e., when j_x departs from the $\langle 111 \rangle$ towards the $\langle 110 \rangle$ direction, and they finally tend to assume a shape which is specular with the $\delta\psi > 0$ case but characterized by an abnormally large value of $|\vartheta_z|$ (compare Curves 6 and 11 in Fig. 5.11). The existence of more than one value of ϑ_z for a fixed E_x is limited to a narrow range of values of $\delta\psi$. Already for $\delta\psi = 3{,}64°$, as represented by Curve 6, we find only a region with anomalously great, but everywhere monovalued, Sasaki fields.

Varying the parameters η and τ_0^{-1} brings the result that the region of E_x, characterized by the existence of nontrivial solutions, smoothly decreases with increasing intervalley impurity scattering (especially on the low-field side). The above region of E_x is also diminished at increasing intervalley scattering with TA phonons, but with a more specific dependence on the different f type phonons.

5.4.3 Numerical Results for the Drift Velocity

The numerical values for the drift velocities as functions of the applied field [5.15, 19] are reported in Fig. 5.12 for various directions. The calculations were performed by using $\eta = 0.1$ and $\tau_0^{-1} = 10^8\ s^{-1}$ for all orientations except the

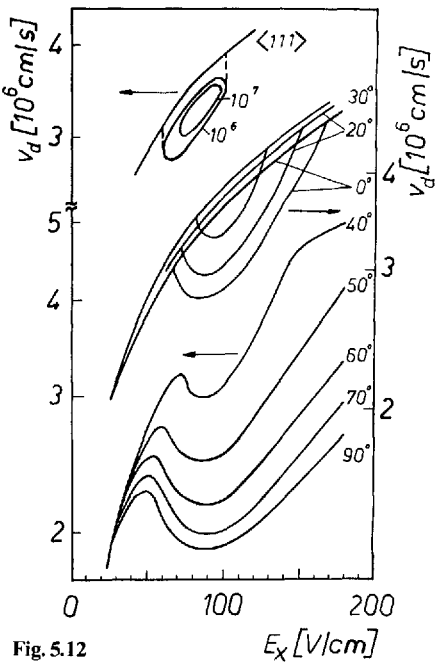

Fig. 5.12

Fig. 5.12. Calculated drift velocities versus field for the indicated orientations at 27 K

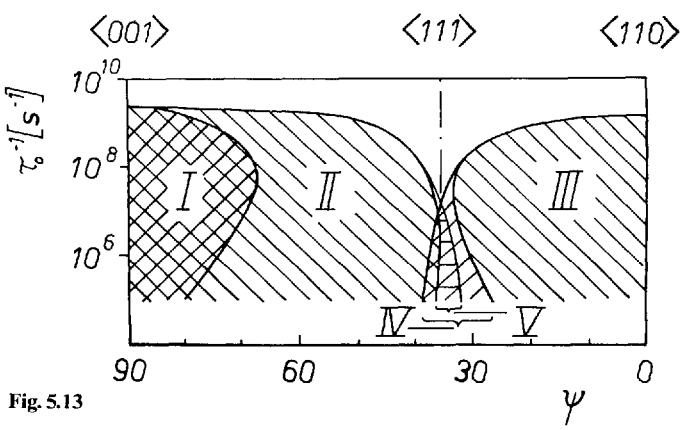

Fig. 5.13

Fig. 5.13. Regions for the existence of different types of NDC and MED (see text) as functions of the current-density orientation in the plane $(\bar{1}10)$ and of the impurity intervalley scattering time. Calculations are performed for 27 K with $\eta = 0.1$

⟨111⟩ direction, for which the values of intervalley impurity scattering rate are indicated in s^{-1} units.

For orientations lying between ⟨110⟩ and ⟨111⟩ directions – Region III in Fig. 5.13 – a state with equally populated Valleys 1 and 2 is not stable and the effect of MED is exhibited by the lower branches of the curves, while the upper ones refer to the case of shunted ϑ_y.

For orientations lying between ⟨111⟩ and ⟨001⟩ directions, NDC is observed because of the predominant population of Valleys 3. Partly this is

connected with the term $\Phi a_1 (1 - 3 \cos 2\psi)/4$ in (5.6), which describes the change of the effective masses along the direction of the applied field due to the intervalley transfer (Region I in Fig. 5.13). Such an effect was known long ago for n-GaAs [5.6, 7], as well as for n-Ge along a ⟨111⟩ direction [5.8] and for n-Si along a ⟨001⟩ direction (see [5.14], for instance). On the other hand, in (5.6) there are terms with ϑ_z, which dominate if j_x is declining remarkably from the direction of the symmetry axis of one valley (Region II in Fig. 5.13).

For orientations very close to the ⟨111⟩ direction, theory predicts that MED should lead to velocity-field curves in the form of isolated loops (Fig. 5.12) with correspondent closed loops for the transverse field, as already mentioned in Sect. 5.3.3. Whether or not these loops contribute to the current-voltage characteristics depends on the boundary conditions [5.15, 17]. In the absence of intervalley relaxation on the surface and for an inhomogeneous field distribution, solutions can exist for which the loops lead to a N-type NDC (broken lines indicated in Fig. 5.12). In Fig. 5.13 the Region IV is ascribed to loops due to the MED between the Valleys 1 and 2, and the Region V is ascribed to loops due to the MED between the Valleys 3 and either of the Valleys 1 or 2, respectively. Very close to a ⟨111⟩ direction, when $\eta = 0.1$, NDC disappears already for values of τ_0^{-1} between 10^7 and $10^8\ s^{-1}$, i.e., for these orientations MED requires a crystal purity higher than for any other orientation, as shown in Fig. 5.13.

Similar investigations for a (100) plane can be found in [5.15, 19].

5.5 Low Temperature as Condition for MED

The considered symmetry breaking requires a steep increase of the intervalley scattering rate at increasing field, as can be seen from the logarithmic derivative in (5.13, 17). This condition is achieved in practice when the carrier temperature is lower than the equivalent temperature of the phonon involved in the transition. In fact, as can be seen from Figs. 5.9 and 5.14, at increasing electric field strength the dependence of $\tau^{-1}(E^{(\alpha)})$ on electric field becomes smoother and, in turn, only the trivial solution will exist.

With rising lattice temperature the effect of carrier heating on the repopulation rate becomes less pronounced, as shown in Fig. 5.14. Accordingly, in comparison with the results at 27 K (Sect. 5.3.2), the numerical calculations [5.15, 19] for the ⟨110⟩ direction show a remarkable weakening of the MED effect at temperatures above 40 K, and predict that the MED effect vanishes above 50 K.

Experimental results of the current density versus applied electric fields [5.21, 22] are shown in Fig. 5.15. Here the arrows indicate the values of the threshold field for the current saturation. It is clearly shown that this value systematically increases with increasing temperature, especially above 40 K, and that the effect of current saturation vanishes for $T_0 > 50$ K. These results are in agreement with the numerical calculations performed with $\eta = 0.1$ and $\tau_0^{-1} \gtrsim 10^7\ s^{-1}$.

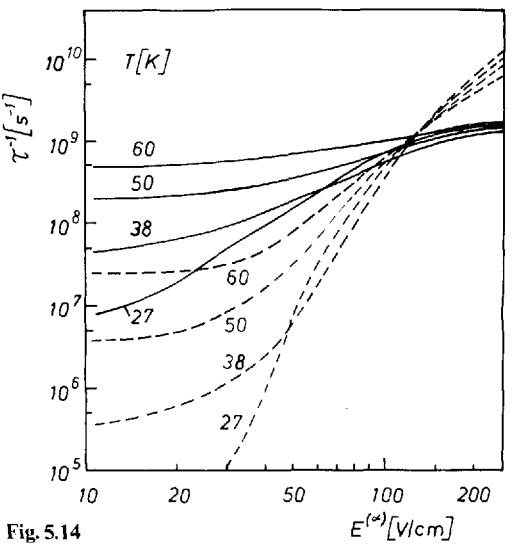

Fig. 5.14

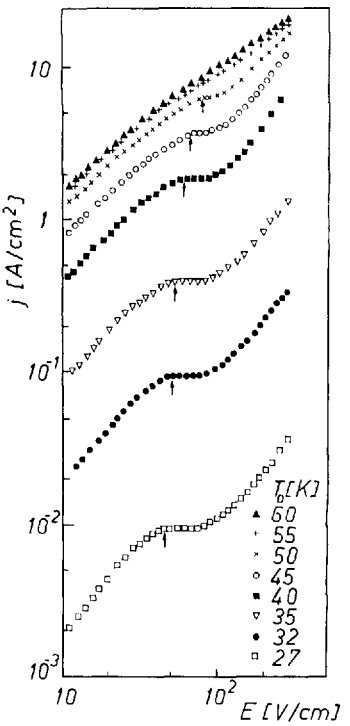

Fig. 5.15

Fig. 5.14. f-type intervalley scattering rates versus effective-field strength for TA phonons (——) and LA plus TO phonons (– – – –) for the indicated temperatures

Fig. 5.15. Current densities versus field applied along the ⟨110⟩ direction at the indicated temperatures

Concerning the effect of the lattice temperature on the transverse fields, it is found from experiments that the presence of a magnetic field parallel to a ⟨001⟩ direction (Sect. 5.2.1) permits one to analyze the involved dependences in a better way because spurious effects, which may influence the position of the interlayer wall, can be excluded. Therefore the potential difference ΔU_{12} measured between probes on opposite $(\bar{1}10)$ surfaces will be ascribed to the transverse field strength in a more reliable way. Values of $\Delta U_{12}/d_{12}$ (see insert of Fig. 5.2) are reported in Fig. 5.16 [5.21] as a function of $\boldsymbol{B}$ for $E_x = 106$ V/cm (for this value of the applied field there is no longitudinal domainization due to NDC) at the indicated lattice temperatures. One can see that for $T_0 \leq 50$ K the steep rise in the region of weak $\boldsymbol{B}$ coincides for all curves with MED. Furthermore, the value of the transverse field measured at high $\boldsymbol{B}$ is found to decrease for T_0 above 40 K.

For $T_0 > 50$ K the change of slope, from the steep rise at weak $\boldsymbol{B}$ to the smooth rise at strong $\boldsymbol{B}$, becomes more broadened than at lower temperatures.

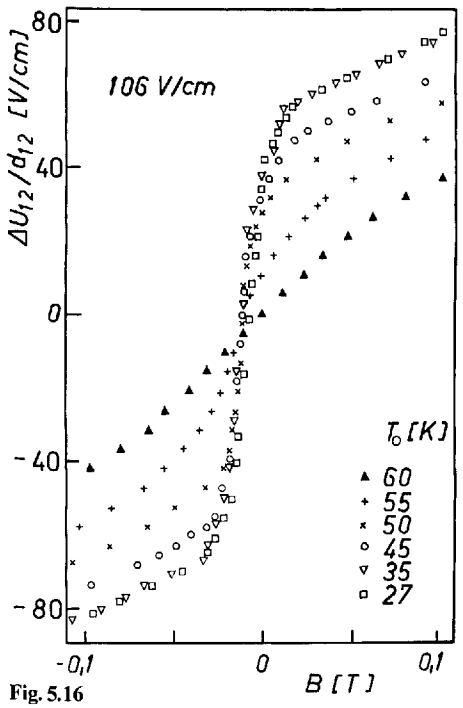

Fig. 5.16

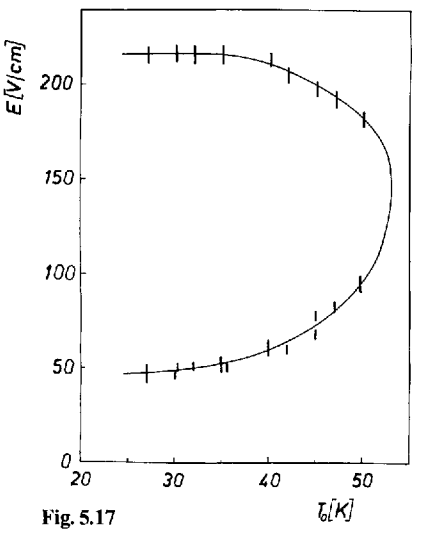

Fig. 5.17

Fig. 5.16. Transverse electric fields versus magnetic field as measured at the indicated temperatures

Fig. 5.17. Region of applied fields and lattice temperatures for the existence of MED as obtained from experiments with E_x along a ⟨110⟩ direction

Furthermore, above 55 K the initial steep rise, due to the switching of the wall, disappears and only an anomalously strong Hall effect is observed [5.12]. Consequently, *the existence or absence of this abrupt change in slope, as exhibited by the transverse field versus magnetic field, can be taken as a criterion for the existence or absence of* MED. When this criterion is applied to n-Si for a current density along a ⟨110⟩ direction, the values reported in the upper part of Fig. 5.17 are obtained for the existence of MED [5.22].

5.6 Experimental Results in Si for a Current Density Nonsymmetrically Oriented

5.6.1 Multivalued Transverse Fields for Current Densities Between ⟨110⟩ and ⟨111⟩ Directions

Due to the carrier redistribution between the Valleys 1 and 2, multivalued transverse fields are possible for orientations of the current density which range

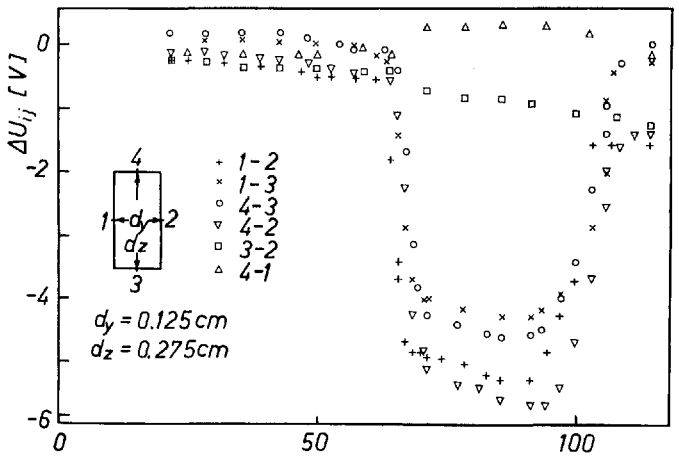

Fig. 5.18

Fig. 5.18. Potential differences, measured between the probes indicated in the insert, versus applied field for $\psi = 33.5°$ at 27 K

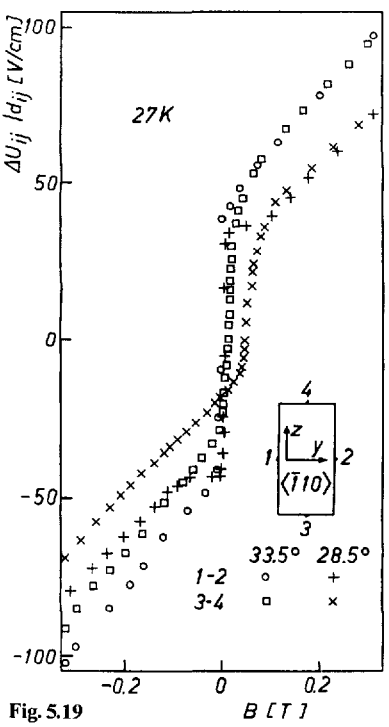

Fig. 5.19

Fig. 5.19. Transverse electric fields E_y and E_z versus magnetic field as measured at the indicated orientations of E_x (ψ counted from ⟨110⟩ towards ⟨111⟩ direction)

from ⟨110⟩ up to nearly ⟨111⟩ directions. In contrast with the ⟨110⟩ direction, in the vicinity of the ⟨111⟩ direction an electron repopulation into either Valleys 1 or 2 leads to transverse fields with components parallel or opposite to E_y, respectively, and E_z (but equal in sign in both cases).

Figure 5.18 reports the values of the potential differences, measured between the probes indicated in the insert, as functions of the heating field for an orientation of the current density departing by $\psi = 33.5°$ from the $\langle 110 \rangle$ direction.

With the exception of ΔU_{32} and ΔU_{41}[8], the potential differences appear and vanish sharply at fixed values of the applied field. Furtheron it is noticed that the region of heating fields where high transverse fields appear is significantly smaller than for the $\psi = 0$ case. These observations indicate the presence of loops, theoretically predicted for both the transverse field and the current density close to the $\langle 111 \rangle$ direction (see Region IV in Fig. 5.13), in contrast with the small Sasaki fields expected in the absence of MED.

Again the existence of MED can be clearly evidenced by applying a magnetic field perpendicular to the current density as well as to the investigated transverse field component E_y, and then, analyzing with the criterion reported at the end of Sect. 5.5, how the potential difference between probes on opposite $(\bar{1}10)$ surfaces is influenced. As shown in Fig. 5.19, an abrupt change of the potential difference ΔU_{12} is observed at increasing values of $\boldsymbol{B}$ parallel to $\hat{z}$ for both the sample orientations. This exhibits how the wall between the regions with predominant population of either Valley 1 or 2 is shifted between the $\langle \bar{1}10 \rangle$ surfaces. At the same time, a measurement of ΔU_{34} in dependence on B_z shows no change. This is expected due to the mere interchange of the roles of Valleys 1 and 2 for this configuration.

In agreement with theory (see Region V of Fig. 5.13) experiments show that the MED between Valleys 1 plus 2 and Valleys 3 is possible for orientations of the current density very close to the $\langle 111 \rangle$ direction in very pure samples. Otherwise, the same effect can be achieved by applying $\boldsymbol{B}$ along the $\langle 1\bar{1}0 \rangle$ direction, since in this case the total electric field vector is turned towards the $\langle 001 \rangle$ direction. This time the potential difference ΔU_{34} is very sensitive to a change of the value of $\boldsymbol{B}$ around a critical value, corresponding to the sudden repopulation from Valleys 1 or 2, respectively, into the Valley 3. This value is higher for greater deviations of the current vector from $\langle 111 \rangle$ towards $\langle 110 \rangle$ directions; see Fig. 5.19 for 28.5°. At this critical value of B_y, ΔU_{12} jumps from its value due to the transverse fields E_y in the case of the population of one of the Valleys 1 or 2 to zero.

5.6.2 Current-Voltage Characteristics in the $(\bar{1}10)$ Plane

According to the theoretical considerations of Sect. 5.4.3, at low lattice temperatures and for not too high scattering rates on ionized impurities, NDC in the current-voltage characteristics should be observed for almost every orientation of the current density in the $(\bar{1}10)$ plane. This expectation had been verified

8 Both the pairs of Probes 3 and 2 as well as 4 and 1 lie almost on equipotential lines, because, for the sample considered above, the interlayer wall is not located in the middle of the sample, but near the surface.

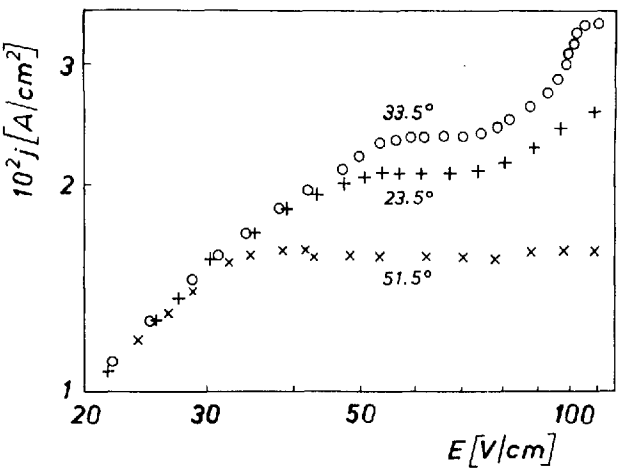

Fig. 5.20. Current density as a function of applied electric field for the indicated orientations at 27 K. Angles are measured from ⟨110⟩ direction in the ($\bar{1}$10) plane

first for the case of orientations between ⟨001⟩ and ⟨111⟩ directions. In this case the combined effects of the change of effective mass of the total carrier ensemble in the current direction as due to electron redistribution between the valleys and of the transverse fields occur (Region II in Fig. 5.13). On the other side, for the case of orientations between ⟨111⟩ and ⟨110⟩ directions, when MED is realized (Regions III and IV in Fig. 5.13), the existence of NDC was verified, too. Typical experimental results are reported in Fig. 5.20. Here, as expected, for both cases a saturation of the current density is observed. This occurs because the NDC leads to the appearance of static high-field domains, as proved experimentally by measuring the potential drop along the sample. Only for the ⟨111⟩ direction the saturation effect has not been detected. Probably the reason is that even at the small acceptor concentration of 5×10^{12} cm^{-3}, the value of τ_0^{-1} is not low enough for NDC to occur in this direction (Fig. 5.13). Otherwise, the experimental results compare well with numerical data when values of τ_0^{-1} in the range from 10^7 to 10^8 s^{-1} are used [5.19]. The different origins of NDC for orientations between ⟨001⟩ and ⟨111⟩ directions and between ⟨111⟩ and ⟨110⟩ directions can be evidenced by the influence of magnetic fields.

5.7 Conclusion: Historical Survey and Future Investigations

The MED among equivalent valleys treated in the present chapter was at the origin of a triple-valued dependence of the Sasaki field, theoretically predicted in 1962 by *Reik* and *Risken* [5.23] in n-Ge when the current density was oriented near a ⟨110⟩ direction for the limiting case of negligible intervalley scattering.

However, these authors paid no attention to this effect, since it vanished for an appropriate choice of the scattering rate which provided better agreement between experimental and numerical results.

The problem of the possible existence of multivalued transverse fields was theoretically considered in 1970 by *Gribnikov* et al. [5.3], and the first experimental indication with respect to this subject was reported in 1972 by *Astrov* and *Kastalskii* [5.29]. In the mean time, most of the interest was devoted to the similar problem of the transverse negative resistance [5.24–28]. These authors, recognizing the necessity of a strong intervalley repopulation rate, required in [5.3], performed measurements in Ge at low temperatures. By choosing the heating field along a ⟨100⟩ direction, they investigated the electric response in the ⟨110⟩ direction for both the closed and open circuit conditions. In a certain region of applied fields, they observed the appearance of transverse potential differences, which they correlated with MED on account of fluctuations. The experimental data, however, do not allow one to draw such conclusions unambiguously [5.15].

Early attempts to measure transverse instabilities in n-Si were made in 1972 by *Gram* et al. [5.30]. However, their efforts were unsuccessful because the lattice temperature they chose was not low enough to satisfy the required steep increase of the intervalley repopulation rate with heating field strength.

As reported in this chapter, the existence of MED has been definitely confirmed in recent years. Therefore, in perspective its consequences with respect to other phenomena should open fruitful areas of investigation. These pertain to the optical properties with the interaction of light with free carriers as well as microwave transduction phenomena probably accompanied by resonances.

Acknowledgement. I want to thank Prof. Dr. O. G. Sarbey for valuable discussions and Dr. H. W. Streitwolf and Dr. L. Reggiani for a critical reading of the manuscript.

References

5.1 H.Haken: *Synergetics, An Introduction*, 3rd. ed., Springer Ser. Syn., Vol. 1 (Springer, Berlin, Heidelberg 1983)
5.2a M.Shibuya: Phys. Rev. **99**, 1189–1195 (1955);
5.2b W.Sasaki, M.Shibuya: J. Phys. Soc. Jpn. **11**, 1202–1203 (1956)
5.3 Z.S.Gribnikov, V.A.Kochelap, V.V.Mitin: Zh. Eksp. Teor. Fiz. **59**, 1828–1845 (1970)
5.4 Z.S.Gribnikov, V.V.Mitin: Zh. Eksp. Teor. Fiz. Pisma **14**, 272–276 (1971), Phys. Status Solidi (b) **68**, 153–164 (1975)
5.5 B.K.Ridley, T.B.Watkins: Proc. Phys. Soc. Lond. **78**, 293–304 (1961)
5.6 C.Hilsum: Proc. IRE **50**, 185–189 (1962)
5.7 J.B.Gunn: J. Phys. Soc. Jpn. **21**, 505–508 (1966)
5.8 A.A.Kastalskii, S.M.Ryvkin: Zh. Eksp. Teor. Fiz. **7**, 446–450 (1968)
5.9 M.Asche, H.Kostial: Solid State Commun. **39**, 457–460 (1981)
5.10 Z.S.Gribnikov, V.V.Mitin: Fiz. Tekh. Poluprov. **9**, 276–281 (1975)
5.11 M.Asche, H.Kostial, O.G.Sarbey: J. Phys. **C13**, L645–649 (1980)
5.12 M.Kriechbaum, H.Heinrich, J.Waida: J. Phys. Chem. Sol. **33**, 829–838 (1972)
5.13 M.Asche, H.Kostial: Phys. Status Solidi (b) **93**, K89–92 (1979)

5.14 L.F.Kurtenok, E.A.Movchan, O.G.Sarbey, V.V.Mitin, M.Asche: Phys. Status Solidi (a) **48**, 323–328 (1978)
5.15 M.Asche, Z.S.Gribnikov, V.V.Mitin, O.G.Sarbey: *Gorjachie electroni v mnogodolinnikh poluprovodnikakh* (Naukova dumka, Kiev 1982) Chap. 3
5.16 H.F.Budd: Phys. Rev. **131**, 1520–1524 (1963)
5.17 Z.S.Gribnikov, V.M.Ivashchenko, V.V.Mitin, O.G.Sarbey: *Chislennii raschet mnogosnachnikh raspredelenii elektronov po dolinam* (preprint No **8**, Inst. Fiz. AN, Kiev 1981)
5.18 M.Asche, Z.S.Gribnikov, V.M.Ivashchenko, H.Kostial, V.V.Mitin, O.G.Sarbey: Zh. Eksp. Teor. Fiz. **81**, 1347–1361 (1981)
[English transl.: Sov. Phys. – JETP **54**, 715–722 (1982)]
5.19 M.Asche, Z.S.Gribnikov, V.M.Ivashchenko, H.Kostial, V.V.Mitin: Phys. Status Solidi (b) **114**, 429–438 (1982)
5.20 M.H.Jørgensen: Phys. Rev. **B18**, 5657–5666 (1978)
5.21 M.Asche, H.Kostial, O.G.Sarbey: J. Physique **42**, C7-323–328 (1981)
5.22 H.Kostial, L.F.Kurtenok: Phys. Status Solidi (b) **109**, K109–113 (1982)
5.23 H.A.Reik, H.Risken: Phys. Rev. **126**, 1737–1746 (1962)
5.24 E.Erlbach: Phys. Rev. **132**, 1976–1979 (1963)
5.25 M.Shyam, H.Kroemer: Appl. Phys. Lett. **12**, 283–285 (1968)
5.26 C.Hammar: Phys. Rev. **B4**, 2560–2566 (1971)
5.27 N.N.Grigorev; I.M.Dykman, P.M.Tomchuk: Fiz. Tverd. Tela **8**, 1083–1089 (1974)
5.28 T.K.Gaylord, T.A.Robson: Phys. Lett. **38A**, 493–494 (1972)
5.29 Ju.A.Astrov, A.A.Kastalskii: Fiz. Tekh. Poluprov. **6**, 323–328 (1972)
5.30 N.O.Gram, M.N.Jørgensen, N.I.Meyer: Proc. 11th Intern. Conf. Phys. Semicond., Warsaw, Poland, 1972 (PWN, Warsaw 1973) pp. 622–629.